The Impact of Surface Composition on the Interfacial Energetics and Photoelectrochemical Properties of $BiVO_4$

Dongho Lee,[1,#] Wennie Wang,[2,#] Chenyu Zhou,[3,4,#] Xiao Tong,[3] Mingzhao Liu,[3,*] Giulia Galli,[2,5,6*] and Kyoung-Shin Choi[1,*]

[1]*Department of Chemistry, University of Wisconsin-Madison, Madison, WI 53706, United States*
[2]*Pritzker School of Molecular Engineering, University of Chicago, Chicago, IL 60637, USA*
[3]*Center for Functional Nanomaterials, Brookhaven National Laboratory, Upton, NY 11973, United States*
[4]*Department of Materials Science and Chemical Engineering, Stony Brook University, Stony Brook, NY 11794, United States*
[5]*Department of Chemistry, University of Chicago, Chicago, IL 60637, USA*
[6]*Argonne National Laboratory, Lemont, IL 60439, USA*

[#] These authors contributed equally.

* Correspondence and requests for materials should be addressed to G.G. (email: gagalli@uchicago.edu), M.L (email: mzliu@bnl.gov), and K.-S.C. (email: kschoi@chem.wisc.edu).

Abstract

The ability to engineer the photoelectrode surface is pivotal for optimizing the properties of any photoelectrode used for solar fuel production. Altering crystal facets exposed on the surface of photoelectrodes has been a major strategy to modify their surface structure. However, there exist numerous ways to terminate the surface even for the same facet, which can considerably alter the photoelectrode properties. This study aims to demonstrate and develop an understanding of the remarkable impacts of surface termination/composition of the same facet on interfacial energetics and photoelectrochemical properties using epitaxial $BiVO_4$ photoelectrodes with V-rich and Bi-rich (010) facets. Using well-defined experimental samples and matching surface structural models, tightly integrated experimental and computational investigations were performed to elucidate the microscopic origins of how the surface termination and composition affect the photoelectrochemical properties. This study opens an unexplored path for understanding and engineering surface energetics via tuning the surface termination/composition of multinary oxide photoelectrodes.

Photoelectrochemical water splitting presents an attractive strategy to produce hydrogen gas as an alternative clean fuel in an environmentally benign and sustainable manner[1–3]. The key component of a photoelectrochemical cell is a semiconductor electrode (photoelectrode) that absorbs solar light to generate, separate, and transport charge carriers to the semiconductor/electrolyte interface to participate in desired chemical reactions[4]. The electron-hole separation and interfacial charge transfer of the photoelectrode are considerably affected by the interfacial energetics between the photoelectrode and the electrolyte and/or between the photoelectrode and the buffer, protection, or catalyst layers[2,5–9]; hence, the interfacial properties of a photoelectrode are as important as the bulk properties of the photoelectrode.

To date, strategies for altering the atomic arrangement at the photoelectrode surface that do not involve extrinsic doping have mainly involved changing the semiconductor surface facets[10,11]. However, for ternary oxide photoelectrodes with a formula of $A_xB_yO_z$, there exist numerous ways to terminate the surface even for the same facet. For example, the surface can be terminated with A-O or B-O, and the surface A:B ratio may be different from the bulk A:B ratio. In fact, if not grown as single crystals, $A_xB_yO_z$ photoelectrodes can have an A-rich or B-rich surface depending on the synthesis method, which can affect their photoelectrochemical properties. However, despite being important and ubiquitous, the effects of surface termination/composition on a ternary oxide photoelectrode have not been systematically studied, and the atomic origin of their effects on interfacial energetics and photoelectrochemical properties have not been elucidated. This lack of study can be attributed to the fact that gaining such a microscopic understanding requires tightly integrated experimental-computational studies that must meet numerous requirements to obtain meaningful and reliable results as summarized below.

First, samples with at least two different, well-defined surface compositions/structures must be prepared as *electrodes.* These electrodes must have the same bulk composition/structure/orientation so that any differences observed in the surface energetics and photoelectrochemical properties are solely due to the differences in the surface atom compositions/structures. Additionally, the difference in composition must be only in the surface atomic layers, and the formation of a thick surface layer of binary oxides of A or B (i.e., heterojunctions of $A_xB_yO_z/A_mO_n$ or $A_xB_yO_z/B_mO_n$) must be avoided. Furthermore, the photoelectrodes should have a high photoelectrochemical activity and generate a considerable and reproducible photocurrent so that the difference in photocurrent arising from the difference in surface termination/composition can be unambiguously quantified. Second, realistic surface models that represent the experimental surfaces must be established using a proper level of theory that is capable of accurately describing the surface electronic properties. Third, a procedure must be established to confirm that the surfaces modeled theoretically closely mimic the experimental surfaces. This is not a trivial task; in principle, a plethora of choices for the theoretically modeled surface structure is possible. Fourth, the theoretically predicted and experimentally measured surface energetics must be compared, and the results should closely match to validate the level of theory and the quality of the experimental samples. Lastly, the differences in the surface energetics of the samples should be able to explain the differences in the photoelectrochemical properties of the samples.

The current study is designed to meet all the aforementioned requirements. $BiVO_4$ is chosen as a model ternary oxide photoelectrode as it has been identified as the most promising oxide photoelectrode for photoelectrochemical water splitting[4,12–15]. We studied epitaxially grown $BiVO_4$ (010) photoelectrodes with V-rich and Bi-rich exposed facets. We also computationally modeled V-rich and Bi-rich (010) facets using first-principles calculations whose simulated scanning tunneling microscopy (STM) images match well with the experimental ones. Using well-defined experimental samples and matching surface structural models, here we provide a comprehensive computational and experimental interpretation of the effects of surface termination/composition on the interfacial energetics and photoelectrochemical properties of $BiVO_4$ (010) photoanodes.

Characterization of the epitaxial $BiVO_4$ electrodes

$BiVO_4$ films used in this study were epitaxially grown by pulsed laser deposition on an yttrium-stabilized cubic zirconia (YSZ) substrate coated with a thin epitaxial layer of indium tin oxide (ITO), which makes the substrate electrically conductive. We note that the *hkl* indices used are with respect to the C-centered monoclinic cell (C 2/c) (**Supplementary Fig. 1**)[12]. The X-ray diffraction (XRD) pattern of the resulting $BiVO_4$ film shows only (0*k*0) peaks (**Fig. 1a-b**), confirming that the film has uniformly grown along the [010] direction. The epitaxial nature of the $BiVO_4$ films was confirmed in our previous study by atomic resolution high angle annular dark field scanning transmission electron microscopy and selected area electron diffraction[16]. The surface Bi:V ratio of the as-prepared epitaxial film was examined using low energy ion scattering spectroscopy (LEIS), whose sampling depth is limited to the sample's first atomic layer[17,18]. The surface Bi:V ratio was 43:57, which is slightly V-rich.

To change the atomic termination and prepare a Bi-rich surface of $BiVO_4$, we treated the as-prepared $BiVO_4$ with base (0.1 M NaOH) for 1 min. This process takes advantage of the fact that V on the surface of $BiVO_4$ more readily leaches out in basic solution[19]. The goal of the base treatment was to remove only the outermost V layer without altering the bulk. Thus, the concentration of base and the time of film immersion were carefully optimized to achieve this goal. (The optimal condition can vary depending on the crystallinity, morphology, and the original surface composition of the sample.) After the optimized base treatment, the surface Bi:V ratio was determined to be 79:21 by LEIS, suggesting that the base treatment effectively removed the surface V ions. The Bi:V ratio measured by X-ray photoelectron spectroscopy (XPS) was 53:47. Because XPS has a sampling depth that is deeper than the first atomic layer, the Bi:V ratio determined by XPS is the average Bi:V ratio of the first atomic layer and the next few underlying bulk atomic layers. The fact that the Bi:V ratio measured by XPS is still very close to the stoichiometric 1:1 ratio demonstrates that the base treatment eliminated only the surface V atoms while keeping the stoichiometric Bi:V ratio in the underlying bulk layers.

To ensure that the base treatment did not change the surface morphology or roughness, top-view scanning electron microscopy (SEM) images (**Fig. 1c-d**) and electrochemically active surface areas of the electrodes before and after the base treatment (**Supplementary Fig. 2**) were examined, and they were comparable to each other. Furthermore, XRD patterns showed no changes in peak height and width (**Fig. 1a-b**), and UV-vis spectra showed no changes in absorbance (**Fig. 1e**) before and after the base treatment, which additionally confirmed that the base treatment did not cause any changes in the bulk properties of the $BiVO_4$ electrodes.

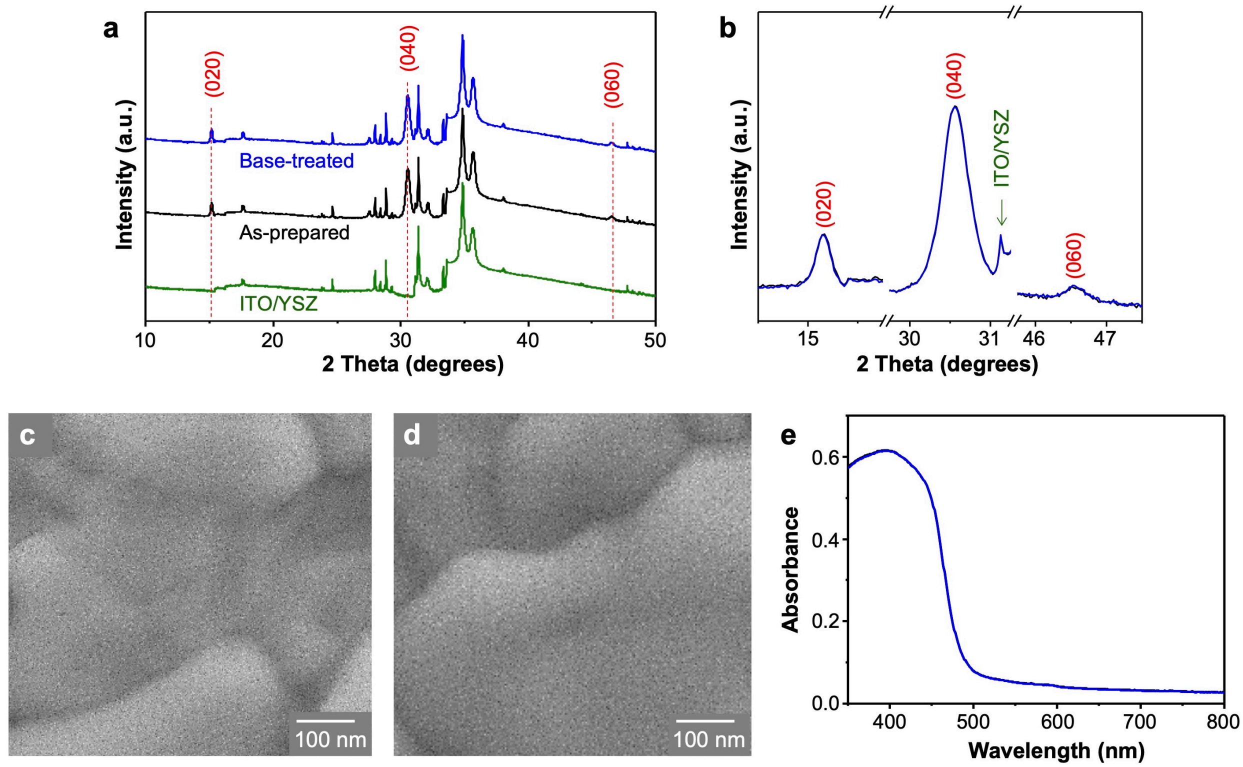

Fig. 1 | Characterization of epitaxial BiVO$_4$ (010) electrodes. **a,** XRD patterns of as-prepared (black) and base-treated (blue) epitaxial BiVO$_4$ electrodes (JCPDS 14-0688). XRD pattern of the ITO/YSZ substrate is shown in green, and (0*k*0) peaks are marked in red. **b,** Magnification of (0*k*0) diffraction peaks in **a**. **c,d,** Top-view SEM images of as-prepared (**c**) and base-treated epitaxial BiVO$_4$ electrodes (**d**). **e**, UV-vis spectra of as-prepared (black) and base-treated (blue) epitaxial BiVO$_4$ electrodes. In **b** and **e**, only blue lines may be visible because black lines coincide exactly with the blue lines.

Surface atomic structure with measured and simulated STM

The most direct evidence that the base treatment successfully altered the surface termination of the epitaxial BiVO$_4$ electrode was obtained by STM. The STM images of the as-prepared and base-treated samples are shown in **Figs. 2b and 2c**, respectively, along with the lattice spacing on the (010) plane from the crystallographic data of BiVO$_4$ (**Fig. 2a)**. It is apparent that the surface features of the two samples are markedly different. The STM image of the as-prepared sample shows distinct rows of uniformly spaced round features. The spacing between bright spots ranges between 4.5 and 5.5 Å, which is comparable with the lattice spacing in the (010) plane (**Fig. 2a**). Representative height profiles are provided in **Supplementary Fig. 3**; the height difference varies between 0.4 and 0.7 Å.

The STM image for the base-treated sample also shows uniformly spaced features, but the bright regions are not round in shape. The distance between the repeating units ranges between 5.0 and 6.0 Å, again close to the lattice spacing in the (010) plane. The difference in height between bright and dark regions varies between 0.8 and 1.1 Å (**Supplementary Fig. 4**).

Next, we compared our measured STM images with ones simulated using density functional theory (DFT). The surface termination models with simulated STM images that closely resemble the measured STM images are shown in **Fig. 2d-f**; 1) the stoichiometric surface consists of fourfold coordinated V tetrahedra and sixfold coordinated Bi polyhedra, 2) the V-rich surface, where the outermost surface Bi are removed and the surface V with initial twofold coordination relax into a compressed fourfold coordination, and 3) the Bi-rich surface in which the outermost surface V are removed and the surface Bi are fourfold coordinated. (More details for determining and choosing these surface models are provided in the Methods section.)

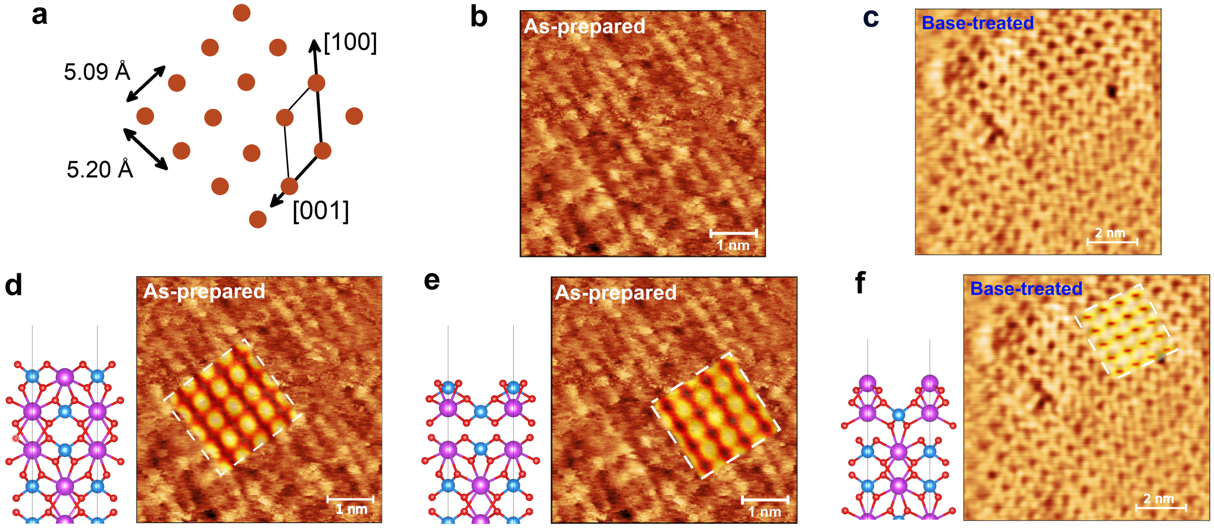

Fig. 2 | Experimental and simulated STM images of $BiVO_4$ (010). a, Schematic of (010) in-plane lattice of $BiVO_4$ oriented with respect to the lattice in the STM images, showing lattice spacing and the C2/c cell convention. **b,c** Measured constant-current STM images of the unoccupied states for the as-prepared (**b**) and base-treated Bi-rich (010) $BiVO_4$ surface (**c**). **d-f,** The simulated constant-current STM images of stoichiometric (**d**), V-rich (**e**), and Bi-rich surfaces (**f**) overlaid (enclosed within white dashed lines) on the measured STM images. The corresponding stoichiometric, V-rich, and Bi-rich slab structures used for the simulations are shown on the side. Bi atoms are purple, V atoms are blue, and O atoms are red.

For the as-prepared sample, we compared the measured STM image with the corresponding simulated images of the stoichiometric and V-rich surfaces **(Fig. 2d-e)**. Both surfaces exhibit the same uniformly spaced bright features, which predominantly correspond to the surface vanadium atoms (see **Supplementary Fig. 5** for the layer-by-layer decomposition of the local density of states at the surface). The spacing of the rounded features coincides with the lattice spacing of the simulation cell, thus allowing us to align the simulated and measured STM images. Both simulated STM images using the stoichiometric and V-rich surface appear comparable to the measured STM image of the as-prepared sample. In our calculations, the height difference between bright and dark regions of the stoichiometric surface is 0.56 Å, which lies comfortably within the range of measured height profiles (0.4 – 0.7 Å); in the V-rich surface, that height difference is 1.4 Å. Thus, in terms of a height profile, the stoichiometric model provides a better fit. This is in agreement with the LEIS result showing that the as-prepared sample is only slightly V-rich.

We next compared the measured STM image of the base-treated Bi-rich sample with a simulated STM image of our Bi-rich surface model (**Fig. 2f**). The bright features predominantly correspond to the unoccupied O 2*p* states that emerge as in-gap defect levels in our calculations (**Supplementary Fig. 5**). The spacing and shape of the pattern in the simulated image again match well with those in the observed image. Notably, the height difference between bright and dark regions in our calculated STM image is 1.23 Å, which is in good agreement with measurements (0.8 – 1.1 Å). From our structural model of the Bi-rich surface, we see that these deeper regions come from the etching of surface V atoms.

The excellent agreement between the measured and simulated STM images confirms that we successfully prepared epitaxial films with V-rich and Bi-rich terminations. These results also confirm that our calculations use representative structural models that closely mimic the surface features of real experimental samples. Hence, we are now in a position to discuss the electronic structure of validated surface structural models and compare with experimental results to reveal the effect of different surface terminations on surface electronic structure.

Electronic structure of varied surface terminations in (010) $BiVO_4$

In our previous study on the (010) $BiVO_4$ surface[20], we demonstrated excellent agreement of band alignment and work function between our calculations of the stoichiometric (010) surface and measurements on single-crystalline samples by Favaro *et al.*[21] In our study, we used DFT with a Hubbard term U to compare surface terminations at the (010) surface, as previous studies have demonstrated DFT+U captures the overall physics of high levels of theory (i.e., hybrid functionals[20,22]).

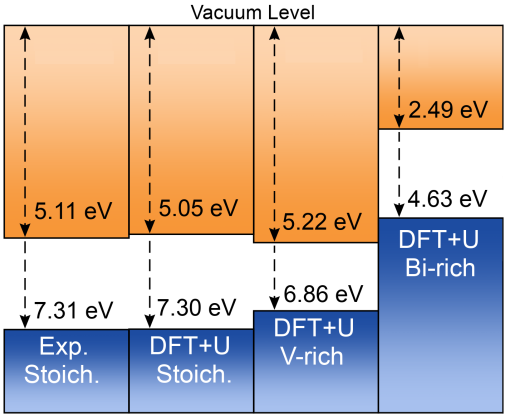

Fig. 3│ Band alignments of $BiVO_4$ (010). Results obtained from calculations at the DFT+U level for the $BiVO_4$ (010) surface with stoichiometric, V-rich, and Bi-rich terminations compared with the experimental results obtained from single-crystal $BiVO_4$ (010) samples[21]. Generated with the help of bapt (https://github.com/utf/bapt).

Band edge positions of V-rich and Bi-rich structures were calculated using the aforementioned surface models (100% V-rich and 100% Bi-rich surfaces) and compared with those of calculated and experimental stoichiometric (i.e., single-crystal) surfaces in **Fig. 3**.

Although experimental V-rich and Bi-rich samples do not exhibit complete loss of Bi or V on the surface, our chosen structural models allow us to understand the maximal difference in electronic structure among different surface terminations and provide meaningful atomistic insights. The greatest change in band edge position for the V-rich surface is the valence band maximum (VBM), which moves up by about 0.4 eV relative to the stoichiometric surface. The Bi-rich surface exhibits a significantly larger shift in the band edge positions toward the vacuum level relative to the stoichiometric surface. Varying the surface Bi richness almost linearly affects the magnitude of the band edge shift (**Supplementary Fig. 6**). We note that our results were obtained with surface models with a limited slab size using surface Bi with only fourfold Bi-O coordination (see Methods for the choice of O surface coordination). Thus, our results are not intended to exactly predict the band edge positions of the experimental samples, which likely possess surface metal ions with more diverse and complex oxygen coordination environments. Instead, our results are meant to present and explain the trend that as the surface Bi content increases, the band edge positions shift toward the vacuum level compared with those of the stoichiometric or V-rich sample. The VBM of stoichiometric $BiVO_4$ is sufficiently more positive (i.e., farther from vacuum) than the water oxidation potential; therefore, the shift of the band edges toward the vacuum level is favorable for overall water splitting as long as the VBM is more positive with respect to the water oxidation potential.

The difference in band edge positions among the stoichiometric, V-rich, and Bi-rich surfaces can be explained using computed average electrostatic potentials. The calculation of electrostatic potentials to align energy levels of surface structural models is a well-established technique in semiconductor physics[23,24]. Energy levels in slabs with different stoichiometries do not have a common zero of energy in our calculations. In order to compare these energy levels, the average electrostatic potentials ($<\tilde{V}>$) felt by the electrons in the bulk-like region of the slabs used to model each surface were computed (dotted lines in **Fig. 4**) and aligned relative to vacuum.

The depth of the average electrostatic potential with respect to vacuum corresponds to the strength of the potential that the electrons experience in the slab. The large shift in band edge positions of the Bi-rich surface toward the vacuum level can thus be understood as mostly arising from the shift in the average electrostatic potential toward the vacuum level. The overall determination of the band edge positions of course includes the details of the surface relaxations and resulting electronic structure (**Supplementary Fig. 5**).

Within each slab, the electrostatic potential of the electrons exhibits variations at the atomic level due to the charge variation around atoms and in bonds. The variation of $\tilde{V}$ along the direction perpendicular to the surface (i.e., [010]) is referred to as the macroscopic electrostatic potential and is represented by the solid lines in **Fig. 4**. We note that the macroscopic electrostatic potential for the V-rich slab *at the surface* exhibits a well at a lower potential compared to that in the bulk-like region (orange arrows in **Fig. 4,** 0.98 eV). A similar potential well exists (black arrows in **Fig. 4**, 0.68 eV) at the surface of the stoichiometric slab and emerges as a consequence of the structural surface relaxations of the (010) surface in $BiVO_4$[20]. The presence of a potential well indicates that electrons tend to accumulate at the surface. A shallower potential well exists at the surface of the Bi-rich slab relative to the bulk region (blue arrows in **Fig. 4**, 0.46 eV), indicating that the depth of the well is largely affected by the presence of surface V and associated surface structural relaxations. The change in $\tilde{V}$ as the function of surface Bi richness can be found in **Supplementary Fig. 7**.

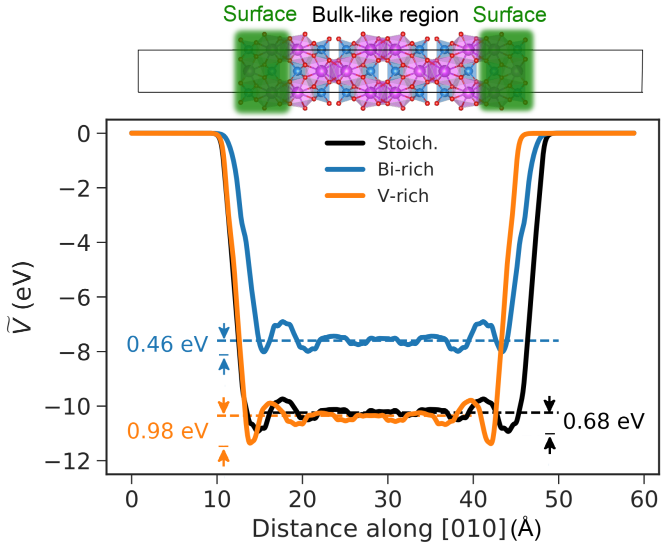

Fig. 4│ Calculated macroscopic electrostatic potentials ($\tilde{V}$) of BiVO$_4$ (010). $\tilde{V}$ (solid lines) for stoichiometric (black), Bi-rich (blue), and V-rich (orange) slabs following the structural models in Fig. 2. A generic slab structure for BiVO$_4$ is shown above, indicating the corresponding surface and bulk-like regions in $\tilde{V}$. The black, blue, and orange dotted lines indicate average $\tilde{V}$ in the bulk-like region, $<\tilde{V}>$, for the stoichiometric, Bi-rich, and V-rich slab structures, respectively. The arrows indicate the depth of the potential difference between $\tilde{V}$ of the surface and of the bulk-like region for each slab structure. The null is taken as vacuum level.

The differences in electronic structure of the stoichiometric, V-rich, and Bi-rich surfaces have several important implications for the photoelectrochemical properties of the (010) surface of BiVO$_4$. First, our results show that even without modifying the atomic planes exposed on the surface, changing the surface termination/composition of the facet can have a considerable effect on the band alignment. This is a profound new insight, as such effects previously could have been expected only through exposing a different facet on the surface[10,11]. **Figs. 3-4** suggest that the base-treated sample with a higher Bi:V ratio can possess a CBM and VBM that are shifted closer to the vacuum level and can have a more favorable band alignment for overall photoelectrochemical water splitting as long as the VBM position remains suitable for water oxidation. Second, the smaller concentration of surface V of the base-treated sample may result in fewer recombination events. It has been reported that electron polarons tend to form on V sites[20,25], whereas hole polarons tend to form on Bi sites[26,27]. Thus, by virtue of having fewer V sites and a shallower potential well, the Bi-rich surface has less tendency for electron polarons to form and recombine with the hole polarons needed for water oxidation.

Next, we examined the effect of surface termination on the work function. The calculated work function of the stoichiometric surface is 5.36 eV, which compares well to the measured work function (5.15 eV) of a single-crystalline BiVO$_4$ doped with ~1 at. % Mo substitutionally for V by Favaro *et al.*[21] We obtained a work function of 6.63 eV for the V-rich surface and 4.06 eV for the Bi-rich surface. As our V-rich surface is constructed with total loss of Bi in the top layer and our Bi-rich surface is with total loss of V in the top layer, our calculated work functions represent two extreme deviations from the stoichiometric one. Thus, the work function of samples with intermediate loss of surface atoms will be between these two extreme values, with the trend that a high surface Bi:V ratio would shift the work function closer to the vacuum level. We note that in these calculations, the surface slabs were modeled as intrinsic semiconductors with no excess carriers. The changes in work function solely originate from the shift of the band edges and from details of the electronic structure of the relaxed slab structure, which affect the density of states and the presence of interband states (**Supplementary Fig. 5**). Thus, these results are not meant to precisely predict the work function of experimental n-type $BiVO_4$ samples but to show the effect of surface Bi:V ratio on the work function even in the absence of any change in the carrier density. Overall, our computational results for the band edge positions and work functions predict that the Bi-rich surface will be able to achieve a more favorable band bending at the $BiVO_4$/electrolyte interface and enhance electron-hole separation.

In order to examine whether the trends observed computationally are also observed experimentally, we measured the work functions and VBMs of as-prepared and base-treated samples using XPS (**Supplementary Fig. 8**). The work functions of the as-prepared and base-treated samples are 4.80 eV and 4.40 eV, respectively. The VBMs of the as-prepared and base-treated samples are 6.38 eV and 6.23 eV, respectively. These results show that the base-treated samples possess a work function and VBM shifted closer to the vacuum level compared with those of the as-prepared ones, which is the trend predicted by our calculations. (As explained previously, the calculated and experimental work function and VBM positions are not expected to match exactly.) We confirmed with XPS that the core level Bi and V peaks do not show any chemical shifts after base treatment (**Supplementary Fig. 9**). Thus, the observed changes are due to the base treatment affecting only the surface Bi:V and not the oxidation states of surface Bi and V ions. Both the computational and experimental results consistently suggest that altering the surface termination of the *same* facet has a considerable impact on the interfacial energetics of $BiVO_4$ and that the Bi-rich (010) surface is more favorable for solar water splitting.

Photoelectrochemical properties of the $BiVO_4$ photoelectrode

To investigate how different atomic terminations of (010) $BiVO_4$ affect the photoelectrochemical properties, J-V plots for sulfite oxidation of as-prepared and base-treated samples were measured in 0.5 M borate buffer containing 0.4 M Na_2SO_3 under AM 1.5G, 100 mW/cm^2 illumination (**Fig. 5a**). Sulfite is a hole scavenger with fast interfacial oxidation kinetics[7,28,29]. Thus, the surface recombination of holes can be assumed to be negligible. As a result, the photocurrent onset potential can reasonably be equated to the flatband potential (E_{FB}) of $BiVO_4$[29]. Also, the difference in photocurrent between the two types of samples can be directly related to the difference in the number of surface-reaching holes, which is a result of the effect of surface termination on interfacial energetics and band bending[29].

We measured J-V plots of six as-prepared and six base-treated samples (**Supplementary Fig. 10**); the average J-V plots with standard deviations are shown in **Fig. 5a**. As these two sets of samples are identical except for the surface termination (**Fig. 1** and **Supplementary Fig. 2**), the observed differences must be due solely to the different surface termination. The results show that the base-treated samples consistently showed significantly higher photocurrent than the as-prepared samples (**Fig. 5a)**. Also, the average photocurrent onset potential (or the average E_{FB}) of the base-treated samples (0.24 ± 0.03 V vs RHE) is shifted to the negative direction compared to that of the as-prepared samples (0.41 ± 0.06 V vs RHE). This result agrees well with the XPS results showing that the work function of the base-treated sample is shifted closer to the vacuum. The difference in the E_{FB} values (0.17 V) is not exactly the same as the difference in the work functions measured with XPS (0.40 eV). This is because E_{FB} is affected not only by the work function but also by the Helmholtz layer potential drop (V_H) at the photoelectrode/electrolyte interface as shown in Eq. 1, where ϕ_{SC} is the work function of the semiconductor and 4.5 V is the scale factor relating the H^+/H_2 redox level to vacuum[1,7]. As shown in Eq. 2, the V_H is affected by the solution pH and the point of zero zeta potential (pH_{PZZP}) of the photoelectrode. The samples with different surface terminations can possess different pH_{PZZP} and, therefore, different V_H values. Thus, the differences in E_{FB} and work function do not need to be the same. Nonetheless, the results shown in **Fig. 5a** agree well with computationally and experimentally determined energetics of the V-rich and Bi-rich $BiVO_4$ (010) photoanodes; the band edge positions and work function of the Bi-rich surface are closer to vacuum and result in more band bending at any given potential, thus producing more surface-reaching holes. These results clearly demonstrate that subtle changes in the surface composition can result in a considerable difference in photocurrent generation.

$$E_{FB}\,(\text{V vs. NHE}) = \phi_{SC}\,(\text{in eV}) + V_H\,(\text{in V}) - 4.5\ \text{V} \qquad (1)$$

$$V_H = 0.059\ \text{V} \times (pH_{PZZP} - pH) \qquad (2)$$

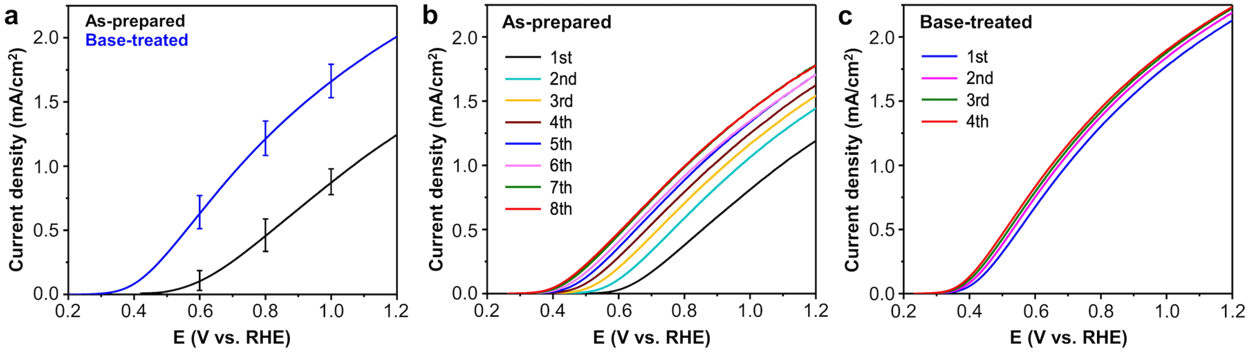

Fig. 5| Photoelectrochemical properties of epitaxial $BiVO_4$ (010) electrodes. a, J-V plots for sulfite oxidation of as-prepared (black) and base-treated (blue) $BiVO_4$ electrodes in 0.5 M borate buffer (pH 9.3) containing 0.4 M Na_2SO_3 under AM 1.5G, 100 mW/cm^2 illumination. The error bars represent standard deviations obtained from measurements of six different samples. **b,c,** Repeated J-V measurements of the as-prepared (**b**) and base-treated $BiVO_4$ electrodes (**c**) under the same conditions.

Since the J-V measurements may change the surface Bi:V ratio and therefore change the surface energetics, we repeated the J-V measurements and examined the corresponding changes in the Bi:V ratio, VBM, and work function of both samples. When the J-V measurements were repeated with the as-prepared sample, the photocurrent onset gradually shifted to the negative direction and the photocurrent continually increased until convergence was reached after the 7th measurement (**Fig. 5b**). The LEIS and XPS analysis after the 1st and 8th J-V measurements revealed that the observed changes were due to the loss of surface V during the J-V measurements, converting the V-rich surface to a Bi-rich surface (**Supplementary Table 1**). The most drastic loss of V occurred during the 1st J-V measurement with the surface Bi:V ratio changing from 43:57 to

79:21; the surface eventually reached an equilibrium Bi:V ratio in pH 9.3 as indicated by the convergence of the J-V plot after the 7th measurement. The increase in the surface Bi:V ratio also affected the VBM and work function positions; both shifted toward the vacuum level (**Supplementary Table 1**) as expected from our calculations. The base-treated sample also showed a slight increase in surface Bi:V ratio during the J-V measurements from 79:21 to 86:14; however, the change in the surface Bi:V ratio and the positions of VBM and work function were considerably less than those observed for V-rich samples. The J-V plots also showed a corresponding small increase in photocurrent, and they converged after the 2nd measurement (**Fig. 5c**). In summary, the LEIS and XPS analyses performed after the J-V measurements of both samples consistently indicate that the surface Bi:V ratio is a key factor affecting the surface energetics and photocurrent generation of $BiVO_4$ even when the two $BiVO_4$ surfaces may undergo additional and different surface reconstructions during J-V measurements.

The J-V plots of the two samples obtained for water oxidation are shown in **Supplementary Fig. 11**, where the photocurrent generated by the base-treated sample is also higher than that of the as-prepared sample. We note that the J-V plots for water oxidation are not as useful as those for sulfite oxidation in studying the effect of the surface composition on surface energetics because the onset potential and photocurrent generation for water oxidation are affected by other factors not directly related to surface energetics (e.g., surface catalytic properties, loss of holes to surface recombination).

Conclusions

In summary, we performed combined experimental and computational investigations using epitaxial $BiVO_4$ photoelectrodes with V-rich and Bi-rich (010) exposed facets and matching surface structural models to understand the impact of surface termination on their interfacial energetics and photoelectrochemical properties. We obtained coherent experimental and computational results that provide new atomistic insights into the relationship between surface termination/composition and photoelectrochemical properties. Our results unambiguously show that the surface Bi:V ratio is a key factor affecting the band edge position and work function: As the surface Bi content increases, these positions shift toward the vacuum level. As a result, the Bi-rich surface has more favorable surface energetics for overall solar water splitting and also produces a higher photocurrent density at any given bias. We found that the changes in the surface Bi:V ratio during photocurrent measurements correlate well with the changes in the band edge positions, work function, and photocurrent generation. Our study represents a critical advancement towards the microscopic understanding of the effect of surface composition in ternary oxide photoelectrodes on their photoelectrochemical properties. We plan to build our understanding of the interfacial energetics of V-rich and Bi-rich $BiVO_4$ (010) further by examining the effect of water and an oxygen evolution catalyst on the surface of $BiVO_4$ in our future studies.

Methods

Synthesis of Epitaxial $BiVO_4$ Films. Epitaxial $BiVO_4$ thin films were deposited on YSZ (010) single-crystalline substrates (MTI Corp) by pulsed laser deposition (PLD) using a KrF excimer laser (λ = 248 nm) operated at a repetition rate of 20 Hz and a fluence of 1.8 J/cm^2. The $BiVO_4$ laser ablation target was prepared by a conventional ceramic sintering method using commercially available $BiVO_4$ powder (Alfa Aesar, 99.9%, ~200 Mesh). To prepare the target, the $BiVO_4$ powder was ground further in an alumina mortar and pressed into a pellet of 30 mm diameter and 5 mm thickness. Finally, the pellet was calcined in air at 700 °C for 10 hours to produce the $BiVO_4$ PLD target. For photoelectrochemical and STM characterizations, a 50-nm-thick ITO film was first deposited over the YSZ substrate at 600 °C under a base pressure of 6×10^{-7} Torr to make the substrate electrically conducting. $BiVO_4$ films were subsequently deposited at 625 °C in 20 mTorr of oxygen. The target-to-substrate distance was maintained at 6 cm. After deposition, the films were cooled down to room temperature under the same atmosphere at a rate of 10 °C min^{-1}. Under these deposition conditions, $BiVO_4$ films grow along the [010] the direction and expose (010) atomic plane on the surface. The crystallographic axes used in this study are based on the C-centered monoclinic cell (C 2/c)[12].

Surface Treatment of $BiVO_4$ Films. To create a Bi-rich surface, the as-prepared $BiVO_4$ film was immersed in 15 mL of 0.1 M NaOH (Sigma-Aldrich, 97%) aqueous solution for 1 min to strip surface vanadium atoms. The base-treated films were rinsed with deionized water (Barnstead E-pure water purification system, resistivity > 18 MΩ cm) and blow-dried with air.

Characterization. STM images were collected from as-prepared and base-treated $BiVO_4$ thin films using an UHV-STM (RHK-7500) with a tungsten tip. Prior to scanning over the $BiVO_4$ samples, the tungsten tip was pre-treated by repeatedly scanning over Au (111). The images were acquired at room temperature under ultra-high vacuum (~10^{-10} torr) at positive bias (electron tunneling from tip to $BiVO_4$ unoccupied states in sample) up to 2.0 V in constant current mode. Scanning at negative bias (electrons tunneling from $BiVO_4$ occupied states to tip) was also carried out but could not produce high-resolution images due to the difficulty in maintaining a stable tunneling current without crashing the tip onto the sample. The failure of image acquisition at negative bias suggests that there are not enough electrons available in occupied states for tunneling into the tip. STM images were post-processed using Gwyddion software (http://gwyddion.net/)[30].

The morphology of the $BiVO_4$ electrodes was examined using SEM (LEO 1530 microscope, Gemini) at an accelerating voltage of 5 kV. The crystallinity and growth orientation of the electrodes were confirmed with XRD (D8 Advance X-ray diffractometer, Bruker) using Ni-filtered Cu K_α-radiation with $\lambda = 1.5418$ Å. Optical absorbances of the electrodes were determined using a Cary 5000 UV-Vis-NIR spectrophotometer (Agilent) with an integrating sphere to simultaneously collect reflectance and transmittance from the electrodes. The VBM and work function of the electrodes were investigated by XPS (K-Alpha X-ray photoelectron spectrometer, Thermo Scientific) using monochromatized Al Kα X-ray (1486.68 eV) as the excitation source. Silver metal was deposited onto the $BiVO_4$ electrode using a Hummer 8.3 DC/RF Sputter System (Anatech USA) to make electrical contact with the electrode. The Fermi edge of the Ar-ion-beam-cleaned silver metal was used as a reference to calibrate the binding energies of the samples. A negative sample bias of -30 V was applied to determine the secondary electron cutoff, the work function, and the $E_F - E_{VBM}$ of the $BiVO_4$ electrodes. Core level XPS spectra were measured with a pass energy of 30 eV, and the surface atomic percentages of the Bi and V were determined from the integrated Bi 4f and V 2p peak areas using Avantage software.

Low energy ion scattering spectroscopy (LEIS). The surface Bi:V ratios of the $BiVO_4$ electrodes were quantified using LEIS with a SPECS IQE 12/38 ion source and a SPECS Phoibos 100 energy analyzer in an ultrahigh vacuum (UHV) chamber. The primary ion is He^+ at a kinetic energy of 1.5 keV, and the scattering angle was fixed at 135°. In LEIS, only the outermost atomic layer significantly contributes to the flux of scattered ions[31]. The kinetic energy of scattered ion, E_s, is given by the following equation using the elastic, 2-body collision approximation[32]:

$$E_s = E_0 \left(\frac{cos\theta \pm \sqrt{(M_2/M_1)^2 - sin^2\theta}}{1+M_2/M_1}\right)^2 \tag{3}$$

in which E_0 is the kinetic energy of the primary ion (1.5 keV), θ is the scattering angle (135°), and M_1 and M_2 are respectively the mass of the primary ion (He^+) and the surface atom (e.g., Bi or V). Based on Eq. 3, the E_s values for Bi and V were determined to be 1405 eV and 1147 eV, respectively. Actual measurements on $BiVO_4$ samples confirmed these values.

The scattered ion flux corresponding to each metal M, S_M, is calculated based on the LEIS peak area, which is further used to calculate the surface atomic coverage ratio.[17] It has been established that for each element M, its surface coverage θ_M is proportional to its LEIS scattering flux S_M, when the matrix effect is negligible,[18] i.e.,

$$\theta_M = \rho_M S_M \tag{4}$$

where ρ_M is the LEIS sensitivity factor of element M. As such, the surface coverage ratio between Bi and V is given by $\theta_{Bi}/\theta_V = \rho_{Bi}S_{Bi}/\rho_V S_V$. Since the value of S_{Bi}/S_V is given directly from the LEIS measurement, the sensitivity factor ratio between Bi and V, ρ_{Bi}/ρ_V, needs to be calibrated to determine the surface coverage ratio θ_{Bi}/θ_V.

To prepare the Bi/V calibration sample, a V foil (Alfa Aesar, 99.8%) was placed in the LEIS chamber and sputtered using Ar ions (2 keV, 7 μA) for 1 hour to strip the surface oxide layer. The foil is subsequently annealed under UHV at 400 °C for 1 hour to desorb Ar atoms from its surface. A pellet of Bi (Sigma Aldrich, 99.999%) was placed next to the V foil and cleaned using Ar ion sputtering (2 keV, 7 μA) for 1 hour and then heated to 200 °C for 1 hour under UHV. At this temperature, Bi sublimes very slowly and condenses on the surface of V foil, forming a submonolayer of adatoms, as observed by LEIS. The surface coverage of bismuth on the V foil varies depending on the distance to the bismuth source (**Supplementary Fig. 12**, scheme on the right). The coverage is higher in the area closer to the Bi source and is much lower in the area far away from it. Since the surface of the Bi/V calibration sample is covered with either Bi or V, the total coverage, $\theta_{Bi} + \theta_V$, equals unity at any point of the sample. Based on Eq. 4, we have $\rho_{Bi}S_{Bi} + \rho_V S_V = 1$, which can be further rearranged as

$$S_{Bi} = \frac{-\rho_V}{\rho_{Bi}} S_V + \frac{1}{\rho_{Bi}}. \tag{5}$$

Essentially, Eq. 5 establishes a linear correlation between the LEIS peak areas of Bi and V, with its slope equaling the negative of the sensitivity factor ratio ρ_V/ρ_{Bi}.

Following this analysis, we measured LEIS spectra at three spots along the gradient of bismuth coverage over vanadium foil (**Supplementary Fig. 12**). Each spot was measured using identical LEIS conditions. As shown in **Supplementary Fig. 13**, there is a very clear linear correlation between the peak areas of the two elements, which validates the assumption of negligible matrix effect and gives the sensitivity factor ratio ρ_V/ρ_{Bi} = 0.253 using linear regression[18]. This sensitivity factor ratio was used to determine the surface Bi:V ratio of our $BiVO_4$ samples.

Photoelectrochemical Characterization. Photoelectrochemical and electrochemical measurements were carried out in an undivided three-electrode cell using an SP-200 potentiostat (Bio-Logic). $BiVO_4$ was used as the working electrode, Pt was used as the counter electrode, and a Ag/AgCl (4 M KCl) reference electrode (RE) was used. The measured potential versus the RE was converted to potential versus the reversible hydrogen electrode (RHE) using the equation below.

$$E\text{ (vs. RHE)} = E\text{ (vs. Ag/AgCl)} + E_{Ag/AgCl}\text{(reference)} + 0.0591\text{ V} \times \text{pH}$$

$$(E_{Ag/AgCl}\text{(reference)} = 0.1976\text{ V vs. NHE at }25^{\circ}\text{C})$$

Simulated solar light was generated using an LCS-100 solar simulator (Oriel) equipped with a 150 W Xe arc lamp and an air mass 1.5 global (AM 1.5G) filter. An infrared filter (Newport) and a focusing lens were placed between the light source and the electrode, and the intensity of light was calibrated to 1 sun (100 mW/cm^2) at the back side of the $BiVO_4$ electrode using an NREL-certified GaAs reference cell (PV measurement). Photoelectrochemical J-V and J-t measurements were taken in 0.5 M borate buffer solution, which was prepared by dissolving 0.5 M H_3BO_3 (Sigma-Aldrich, 99.5%) in DI water and adjusting the pH to be 9.3 using KOH (Sigma-Aldrich, 85%). For sulfite oxidation, 0.4 M Na_2SO_3 (Sigma-Aldrich, ≥ 98%) was added to the 0.5 M borate buffer solution. The photocurrent onset potentials reported in this study are the open circuit potentials of the two $BiVO_4$ electrodes under AM 1.5G illumination in the given electrolyte where the photocurrent density is zero.

Computational Methodology. Our first-principles calculations were based on Kohn-Sham density functional theory (DFT) and used the PBE[33] functional, as implemented in QUANTUM ESPRESSO (QE, v 6.3)[34,35]. We followed the computational methodology of our previous work on the (010) surface[20], highlighting relevant aspects here. We used norm-conserving pseudo-potentials[36,37] with a 90 Ry energy cutoff and a k-point mesh of 4×4×2 for bulk cells. Forces were converged to less than 1 meV/Å. All calculations were spin-polarized and included a Hubbard term (U)[38] correction with U = 2.7 eV applied to the *d* electrons of V sites. Previous studies have demonstrated that the DFT+U approach is appropriate to study defect physics when properly benchmarked against higher level calculations (i.e., calculations using hybrid functionals[22,25] as done in previous work).

In order to model surfaces, we used symmetric slabs[39] generated with Pymatgen[40] and the Atomic Simulation Environment[41] based on the 24-atom cell and a minimum of 8 atomic layers and 20 Å in vacuum. We approximated the monoclinic cell with a tetragonal one for computational convenience; this is a robust approximation as demonstrated in our previous work[20]. The relationship between the I-centered tetragonal cell used for computational study and the C-centered monoclinic cell (C 2/c) of $BiVO_4$ is shown in **Supplementary Fig. 1**. We simulated three surface terminations for the (010) surface. The stoichiometric surface consists of fourfold coordinated V and sixfold coordinated Bi. In order to mimic the Bi-rich (V-rich) surface, we removed surface V atoms (Bi atoms) and relaxed the resulting geometry to within 100 meV/Å. We use a 4×4×1 *k*-point mesh for 1×1×2 supercells (72 atoms) and 2×2×1 *k*-point mesh for 2×2×2 supercells (192 atoms). Simulated STM images were generated using the framework developed by Tersoff and Hamann[42] as implemented in QE. Among the many possible configurations of $BiVO_4$ surfaces, we considered the stoichiometric (010) surface, which contains a 1:1 Bi:V ratio and is known to be one of the lowest energy surfaces[43]. We then removed the the outermost Bi and V atoms from the surface to obtain the V-rich and Bi-rich slab structures, respectively. We note that in a previous work[20] we showed that using an integrated experimental and theoretical strategy, one can successfully describe the band alignment and work function of the stoichiometric (010) surface (including in the presence of oxygen vacancies).

An additional consideration in identifying a structural model for the surface is the coordination of the V and Bi atoms with oxygen. In our calculations, we optimized the internal atomic coordinates of all slabs chosen to represent each surface. For the V-rich surface, we considered a fourfold and twofold coordination of the surface V atoms with oxygen. Based on the comparison of simulated and measured STM images, we eliminated the fourfold coordination and found the twofold coordination to have the best agreement with the measured image. For the Bi-rich surface, we considered configurations with fourfold, fivefold, and sixfold coordination of the surface Bi atoms. We found that the sixfold termination of surface Bi is unstable and the surface Bi tend to relax to have low oxygen coordinations (e.g., fourfold and fivefold configurations). We were able to eliminate the structural model in which all of the surface Bi are fivefold coordinated based on simulated STM images and band alignment calculations. The simulated STM image of the fourfold coordinated surface Bi provides the best fit to the measured one among the structures considered. Nevertheless, as the Bi-O bond is relatively weak, it is plausible that the surface Bi on the experimental surface has a mixture of various oxygen coordinations. In addition, using a 2×2×2 supercell, we verified that this surface structure maintains the 1×1 surface reconstruction, as observed for the stoichiometric (010) surface. We additionally calculated the change in band edge alignment with vacuum as a function of surface Bi content. In order to simulate a Bi-rich surface, we incrementally removed each surface V atom and any associated oxygen atoms (to maintain a fourfold coordination of the surface Bi) at each exposed surface. There are four different surface V sites in our 2×2×2 supercell; we label the removal of one V atom as 25% Bi-rich, the removal of two V atoms as 50% Bi-rich, and so on. Our calculations show a linear dependence of the band edge positions with surface Bi content (**Supplementary Fig. 6**).

In order to calculate the band alignment between different slab structures, we require a common energy reference. As such, we calculated the average electrostatic potential of each of our slab structures and aligned them to vacuum level. We use the implementation available in the QUANTUM ESPRESSO package. The electrostatic potential is defined as the sum of the ionic and Hartree potentials, i.e., the full electron potential excluding many-body electron interactions captured in the exchange-correlation potential. The electrostatic potential contains fluctuations that correspond to the charge variation due to atoms and bonds in the simulation cell. Thus, we performed a planar average perpendicular to the slab surface and a windowing average to arrive at the macroscopic electrostatic potential, $\tilde{V}$. Then we determined the average electrostatic potential in the bulk-like region, $<\tilde{V}>$, of the slab structure and determined the band alignment among different slab structures.

Data availability

The dataset generated and analyzed in the current study are openly available on Qresp[44] (qresp.org) through the University of Chicago node.

Acknowledgments

This work was supported by the National Science Foundation (NSF) under grant no. CHE-1764399. This research used resources of the Center for Functional Nanomaterials, which is a U.S. DOE Office of Science Facility, at Brookhaven National Laboratory under Contract No. DE-SC0012704. This research also used computational resources of the University of Chicago's Research Computing Center. The authors would like to thank Dr. Rachel Farber for helpful discussions in processing STM images.

Author contributions

K.-S.C., G.G., and M.L. supervised the combined experimental and computational investigations. C.Z. prepared epitaxial $BiVO_4$ and performed STM imaging and LEIS analysis of $BiVO_4$ together with X.T. under the supervision of M.L. D.L. performed all other experimental studies of $BiVO_4$ under the supervision of K.-S.C. W.W. performed all computational calculations under the supervision of G.G. All authors discussed the results and contributed to writing the manuscript.

Competing interests

The authors declare no competing interests.

Additional information

Supplementary information is available for this paper.

Reprints and permissions information is available at www.nature.com/reprints.

Correspondence and requests for materials should be addressed to M.L., G.G., and K.-S.C.

References

1. Nozik, A. J. Photoelectrochemistry: Applications to solar energy conversion. *Ann. Rev. Phys. Chem.* **29**, 189–222 (1978).
2. Walter, M. G. *et al.* Solar water splitting cells. *Chem. Rev.* **110**, 6446–6473 (2010).
3. Grätzel, M. Photoelectrochemical cells. *Nature* **414**, 338–344 (2001).
4. Sivula, K. & Van De Krol, R. Semiconducting materials for photoelectrochemical energy conversion. *Nat. Rev. Mater.* **1**, 15010 (2016).
5. Montoya, J. H. *et al.* Materials for solar fuels and chemicals. *Nat. Mater.* **16**, 70–81 (2017).
6. Smith, W. A., Sharp, I. D., Strandwitz, N. C. & Bisquert, J. Interfacial band-edge energetics for solar fuels production. *Energy Environ. Sci.* **8**, 2851–2862 (2015).
7. Kim, T. W. & Choi, K.-S. Nanoporous $BiVO_4$ photoanodes with dual-layer oxygen evolution catalysts for solar water splitting. *Science* **343**, 990–994 (2014).
8. Pham, T. A., Ping, Y. & Galli, G. Modelling heterogeneous interfaces for solar water splitting. *Nat. Mater.* **16**, 401–408 (2017).
9. Nellist, M. R. *et al.* Potential-sensing electrochemical atomic force microscopy for in operando analysis of water-splitting catalysts and interfaces. *Nat. Energy* **3**, 46–52 (2018).
10. Li, D. *et al.* Crystallographic-orientation-dependent charge separation of $BiVO_4$ for solar water oxidation. *ACS Energy Lett.* **4**, 825–831 (2019).
11. Hu, J., Chen, W., Zhao, X., Su, H. & Chen, Z. Anisotropic electronic characteristics, adsorption, and stability of low-index $BiVO_4$ surfaces for photoelectrochemical applications. *ACS Appl. Mater. Interfaces* **10**, 5475–5484 (2018).
12. Park, Y., McDonald, K. J. & Choi, K.-S. Progress in bismuth vanadate photoanodes for use in solar water oxidation. *Chem. Soc. Rev.* **42**, 2321–2337 (2013).
13. Lee, D. K. & Choi, K.-S. Enhancing long-term photostability of $BiVO_4$ photoanodes for solar water splitting by tuning electrolyte composition. *Nat. Energy* **3**, 53–60 (2018).
14. Kuang, Y. *et al.* Ultrastable low-bias water splitting photoanodes via photocorrosion inhibition and in situ catalyst regeneration. *Nat. Energy* **2**, 16191 (2017).
15. Kim, J. H. *et al.* Hetero-type dual photoanodes for unbiased solar water splitting with extended light harvesting. *Nat. Commun.* **7**, 13380 (2016).
16. Zhang, W. *et al.* Anomalous Conductivity Tailored by Domain-Boundary Transport in Crystalline Bismuth Vanadate Photoanodes. *Chem. Mater.* **30**, 1677–1685 (2018).
17. Brongersma, H. H., Draxler, M., de Ridder, M. & Bauer, P. Surface composition analysis by low-energy ion scattering. *Surf. Sci. Rep.* **62**, 63–109 (2007).

18. Cushman, C. V. *et al.* Low energy ion scattering (LEIS). A practical introduction to its theory, instrumentation, and applications. *Anal. Methods* **8**, 3419–3439 (2016).

19. Purbaix, M. *Atlas of Electrochemical Equilibria in Aqueous Solutions*. (National Association of Corrosion Engineers, Houston, 1974).

20. Wang, W. *et al.* The role of surface oxygen vacancies in $BiVO_4$. *Chem. Mater.* **32**, 2899–2909 (2020).

21. Favaro, M. *et al.* Chemical, structural, and electronic characterization of the (010) surface of single crystalline bismuth vanadate. *J. Phys. Chem. C* **123**, 8347–8359 (2019).

22. Seo, H., Ping, Y. & Galli, G. Role of Point Defects in Enhancing the Conductivity of $BiVO_4$. *Chem. Mater.* **30**, 7793–7802 (2018).

23. Bjaalie, L., Himmetoglu, B., Weston, L., Janotti, A. & Van De Walle, C. G. Oxide interfaces for novel electronic applications. *New J. Phys.* **16**, 025005 (2014).

24. Balderschi, A., Baroni, S. & Resta, R. Band offsets in lattice-matched heterojunctions: A model and first-principles calculations for GaAs/AlAs. *Phys. Rev. Lett.* **61**, 734–737 (1988).

25. Kweon, K. E., Hwang, G. S., Kim, J., Kim, S. & Kim, S. Electron small polarons and their transport in bismuth vanadate: A first principles study. *Phys. Chem. Chem. Phys.* **17**, 256–260 (2015).

26. Wiktor, J., Ambrosio, F. & Pasquarello, A. Role of polarons in water splitting: The case of $BiVO_4$. *ACS Energy Lett.* **3**, 1693–1697 (2018).

27. Wiktor, J. & Pasquarello, A. Electron and Hole Polarons at the $BiVO_4$-Water Interface. *ACS Appl. Mater. Interfaces* **11**, 18423–18426 (2019).

28. Reber, J. F. & Meier, K. Photochemical production of hydrogen with zinc sulfide suspensions. *J. Phys. Chem.* **88**, 5903–5913 (1984).

29. Govindaraju, G. V, Wheeler, G. P., Lee, D. & Choi, K. Methods for electrochemical synthesis and photoelectrochemical characterization for photoelectrodes. *Chem. Mater.* **29**, 355–370 (2017).

30. Nečas, D. & Klapetek, P. Gwyddion: An open-source software for SPM data analysis. *Cent. Eur. J. Phys.* **10**, 181–188 (2012).

31. Swartzfager, D. G. Sensitivity Factors for Surface Analysis by Ion Scattering Spectroscopy. *Anal. Chem.* **56**, 55–58 (1984).

32. Smith, D. P. Scattering of low-energy noble gas ions from metal surfaces. *J. Appl. Phys.* **38**, 340–347 (1967).

33. Perdew, J. P., Burke, K. & Ernzerhof, M. Generalized gradient approximation made simple. *Phys. Rev. Lett.* **77**, 3865–3868 (1996).

34. Giannozzi, P. *et al.* Advanced capabilities for materials modelling with QUANTUM ESPRESSO. *J. Phys. Condens. Matter* **29**, 465901 (2017).

35. Giannozzi, P. *et al.* QUANTUM ESPRESSO: A modular and open-source software project for quantum simulations of materials. *J. Phys. Condens. Matter* **21**, 395502 (2009).

36. Hamann, D. R. Optimized norm-conserving Vanderbilt pseudopotentials. *Phys. Rev. B* **88**, 085117 (2013).

37. Schlipf, M. & Gygi, F. Optimization algorithm for the generation of ONCV pseudopotentials. *Comput. Phys. Commun.* **196**, 36–44 (2015).

38. Cococcioni, M. & De Gironcoli, S. Linear response approach to the calculation of the effective interaction parameters in the LDA+U method. *Phys. Rev. B* **71**, 035105 (2005).

39. Sun, W. & Ceder, G. Efficient creation and convergence of surface slabs. *Surf. Sci.* **617**, 53–59 (2013).

40. Ong, S. P. *et al.* Python Materials Genomics (pymatgen): A robust, open-source python library for materials analysis. *Comput. Mater. Sci.* **68**, 314–319 (2013).

41. Hjorth Larsen, A. *et al.* The atomic simulation environment - a Python library for working with atoms. *J. Phys. Condens. Matter* **29**, 273002 (2017).

42. Tersoff, J. & Hamann, D. R. Theory of the scanning tunneling microscope. *Phys. Rev. B* **31**, 805–813 (1985).

43. Zhao, Z., Li, Z. & Zou, Z. Structure and energetics of low-index stoichiometric monoclinic clinobisvanite $BiVO_4$ surfaces. *RSC Adv.* **1**, 874–883 (2011).

44. Govoni, M., Munakami, M., Tanikanti, A., Skone, J. H., Runesha, H. B., Giberti, F., de Pablo, J. & Galli, G. Qresp, a tool for curating, discovering, and exploring reproducible scientific papers. *Sci. Data*, **6**, 190002 (2019).